tvst

Article

# ARCAM-1 Facilitates Fluorescence Detection of Amyloid-Containing Deposits in the Retina

**Kevin J. Cao[1], John H. Kim[1], Heike Kroeger[2,3], Patricia M. Gaffney[2,5], Jonathan H. Lin[2,4], Christina J. Sigurdson[2], and Jerry Yang[1]**

[1] Department of Chemistry and Biochemistry, University of California, San Diego, La Jolla, CA, USA
[2] Departments of Pathology and Medicine, University of California, San Diego, La Jolla, CA, USA
[3] Department of Cellular Biology, Franklin College of Arts and Sciences, University of Georgia, Athens, GA, USA
[4] Departments of Pathology and Byers Eye Institute, Stanford University, Palo Alto, CA, USA
[5] Department of Disease Investigations, San Diego Zoo Wildlife Alliance, San Diego, CA, USA

**Correspondence:** Jerry Yang, University of California, San Diego, Department of Chemistry & Biochemistry, 6100C Pacific Hall, 9500 Gilman Drive, MC 0358, USA. e-mail: jerryyang@ucsd.edu

**Received:** December 3, 2020
**Accepted:** April 14, 2021
**Published:** June 7, 2021

**Keywords:** amyloid; Alzheimer's disease; imaging

**Citation:** Cao KJ, Kim JH, Kroeger H, Gaffney PM, Lin JH, Sigurdson CJ, Yang J. ARCAM-1 facilitates fluorescence detection of amyloid-containing deposits in the retina. Transl Vis Sci Technol. 2021;10(7):5, https://doi.org/10.1167/tvst.10.7.5

**Purpose:** To investigate the use of an amyloid-targeting fluorescent probe, ARCAM-1, to identify amyloid-containing deposits in the retina of a transgenic mouse model of Alzheimer's disease (AD) and in human postmortem AD patients.

**Methods:** Aged APP/PS1 transgenic AD and wild-type (WT) mice were given an intraperitoneal (IP) injection of ARCAM-1 and their retinas imaged in vivo using a fluorescence ophthalmoscope. Eyes were enucleated and dissected for ex vivo inspection of retinal amyloid deposits. Additionally, formalin-fixed eyes from human AD and control patients were dissected, and the retinas were stained using ARCAM-1 or with an anti-amyloid-$\beta$ antibody. Confocal microscopy was used to image amyloid-containing deposits stained with ARCAM-1 or with immunostaining.

**Results:** Four out of eight APP/PS1 mice showed the presence of amyloid aggregates in the retina during antemortem imaging. Retinas from three human AD patients stained with ARCAM-1 showed an apparent increased density of fluorescently labeled amyloid-containing deposits compared to the retinas from two healthy, cognitively normal (CN) patients. Immunolabeling confirmed the presence of amyloid deposits in both the retinal neuronal layers and in retinal vasculature.

**Conclusions:** ARCAM-1 facilitates antemortem detection of amyloid aggregates in the retina of a mouse model for AD, and postmortem detection of amyloid-containing deposits in human retinal tissues from AD patients. These results support the hypothesis of AD pathology manifesting in the eye and highlight a novel area for fluorophore development for the optical detection of retinal amyloid in AD patients.

**Translational Relevance:** This paper represents an initial examination for potential translation of an amyloid-targeting fluorescent probe to a retinal imaging agent for aiding in the diagnosis of Alzheimer's disease.

## Introduction

Alzheimer's disease (AD) is a progressive neurodegenerative disorder affecting 5.8 million Americans aged 65 or older, projected to nearly triple to 14 million by 2060, and is currently one of the top 10 leading causes of death in the US.[1–3] It is characterized by a gradual decline in memory and cognitive skills as well as the appearance of misfolded protein deposits known as amyloids in neuronal tissue. The appearance of amyloids is widely hypothesized to be a central event that is accompanied by neuronal death and occurs long before behavioral symptoms emerge.[4] More recently, independent studies have described the presence of amyloid-containing deposits in the retina of AD patients.[5–8] Clinical studies of patients have also reported changes in vision such as impaired contrast sensitivity and visual acuity as well as diminished perception and the emergence of visual hallucinations.[9,10] Examinations of the retinal architecture reveal reductions in melanopsin containing retinal

ganglion cells in the ganglion cell layer (GCL) that govern circadian rhythm and a pathological thinning of the nerve fiber layer (NFL).[5,11–14] Taken together, these results suggest a potential link between AD pathology in the retina and other clinical manifestations of the disease.

As an extension of the nervous system, the retina provides an ideal setting to screen for neurological disease preceding symptoms at the cellular level, as it is relatively easy to examine with noninvasive optical imaging techniques. Currently, most clinical methods that have been deployed to study ocular changes in AD have provided macrolevel structural and functional information about the retina in patients exhibiting AD symptoms. Optical coherence tomography (OCT) and electroretinography (ERG), for example, have shown changes in retina thickness[5,13,15] and optic nerve function[16,17] but have not shed light on the underlying molecular mechanisms that may cause these changes. In contrast, fundus imaging (ophthalmoscopy) can scan a large area of the retina, providing detailed spatial information about the health of the tissue. Coupled with fluorescence imaging, which can provide high contrast images of anatomical features using fluorescent labels, fundus imaging has become a common tool in vision research. Recent reports have shown that curcumin labels amyloid plaques in the retina.[6,18] Curcumin is a small molecule fluorophore naturally found in turmeric with known amyloid-binding capabilities.[19] When given to transgenic AD mice and human AD patients, it fluorescently labeled amyloid-containing deposits in the retina that could be detected by fluorescence fundus imaging.[6,18] These recent studies highlight an opportunity for development of novel amyloid-targeting fluorophores for detection of retinal amyloid deposits.

We have previously shown the utility of an amyloid-binding fluorescent dye, ARCAM-1 (Fig. 1a), in detecting amyloid aggregates in biofluids.[20,21] ARCAM-1 is a fluorescent probe that binds misfolded protein aggregates such as $\beta$-amyloid (A$\beta$) (Fig. 1a).[20] When bound to A$\beta$, this dye emits maximal fluorescence between 515 and 525 nm, overlapping in fluorescence properties with common bandpass filters for ophthalmic dyes such as fluorescein. Here we present our initial findings that ARCAM-1 can fluorescently stain amyloid-containing deposits selectively in transgenic mouse and human AD brain tissue. We also show that ARCAM-1 can aid in fluorescent antemortem detection of amyloid-containing deposits in the retina of the APP/PS1 mouse model of AD,[22] and for postmortem detection of amyloid-containing deposits in the retina of human AD patients. Together with the reports of a structurally similar compound

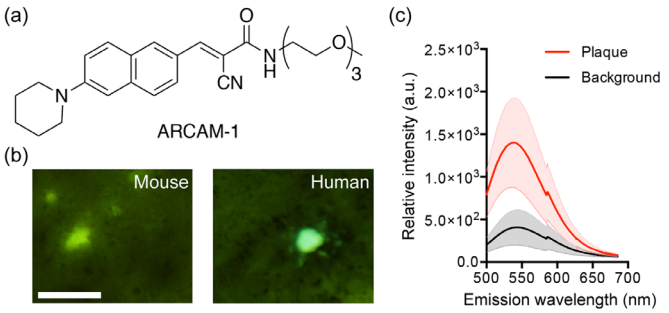


**Figure 1.** ARCAM-1 is an amyloid-staining fluorescent probe. (a) Chemical structure of ARCAM-1. (b) True-color fluorescence micrograph of sections of an APP/PS1 mouse brain and a human Alzheimer's disease patient stained with ARCAM-1. Scale bar = 50 µm. (c) Fluorescence emission spectra of $\beta$-amyloid plaques from a 9-month-old APP/PS1 mouse brain stained with ARCAM-1.

of ARCAM-1, Aftobetin-HCl, which is capable of fluorescently detecting amyloid deposits in the lens of living human AD patients in clinical studies,[23] the results from this study highlight an exciting opportunity for developing novel fluorescent ocular tools to aid in the diagnosis of AD.

# Methods

## Synthesis of ARCAM-1

ARCAM-1 was prepared as previously reported.[20,24] Briefly, we prepared ARCAM-1 via a Buchwald-Hartwig cross coupling reaction between 6-bromo-2-naphthaldehyde and piperidine to give 6-(piperidin-1-yl)-2-naphthaldehyde, which was then condensed with 2-cyano-N-(2-(2-(2-methoxyethoxy)ethoxy)ethyl)acetamide under basic conditions. The product was purified by silica gel chromatography and characterized by $^{1}$H-NMR, $^{13}$C-NMR, and high-resolution mass spectrometry.

## Study Approval

The antemortem in vivo imaging of APP/PS1 mice and related experiments were conducted following an approved protocol from the UC San Diego Institutional Animal Care and Use Committee. Protocols were performed in strict accordance with good animal practices, as described in the Guide for the Use and Care of Laboratory Animals published by the National Institutes of Health. Human patient samples for unfixed frozen brain staining were obtained in accordance with the UC San Diego IRB for human research. Tissue donors were neurologically and psychometrically studied at the Shiley-Marcos Alzheimer's Disease Research Center (ADRC) at UC San Diego. Upon

autopsy, patient brains were collected by the UCSD ADRC Neuropathology Core. Fixed human brain and eye samples were obtained from the University of Miami Brain Endowment Bank in accordance with the university IRB for human research. A total of five postmortem cases (one female and four males) over the age of 70 were examined in this study. Neuropathology of three patients confirmed Alzheimer's disease and two were confirmed cognitively normal. Two out of the three were AD at Braak V/VI while one was low level. Of the two advanced AD cases, one had comorbid Lewy body diseases and Parkinson's disease.

## Antemortem Fluorescence Imaging of Mouse Retinas and Tissue Collection

Fundus images of 11 mice retina (three wild-type and eight transgenic APP/PS1) were obtained using a Micron IV ophthalmoscope (Phoenix Systems) equipped with a long-pass filter (BLP01-488R-25, Semrock) and a CCD camera with 2.0 µm pixel resolution. Mouse pupils were first dilated with 1% tropicamide (Akorn) and 2.5% phenylephrine HCl (Paragon). Mice were then anesthetized with an intraperitoneal (IP) injection of ketamine and xylazine at 10% v/w and placed on a 37°C heating pad. Fluorescence images were obtained before and after an IP injection of ARCAM-1 (100 µL of a 10 mg/mL solution, prepared in 20% DMSO 80% propylene glycol); during imaging, the eyes of each mouse were covered with 2.5% hydroxylpropyl methylcellulose (Hypromellose) ointment (GONAK, Akorn) to prevent dryness and cataract formation. Mice were euthanized by $CO_2$ and cervical dislocation 20 minutes after ARCAM-1 injection. The brain was removed and embedded in optimal cutting temperature medium at –78°C without fixation. The eyes were enucleated with the left eye (OS) placed in 4% paraformaldehyde at room temperature for 2.5 hours and the right (OD) embedded in optimal cutting temperature medium at –78°C without fixation. The retina was dissected from the OS in 1x phosphate buffered saline (1xPBS) and placed in room temperature methanol for 20 minutes and then rinsed in 1xPBS before being mounting to a microscope slide. The OD was cryosectioned at –20°C and sections stored at –80°C prior to staining.

## Staining of Mouse and Human Eye and Brain Tissue

For ARCAM-1 staining of unfixed frozen mouse and human brain sections, slides were first dried for one hour and then hydrated through an ethanol gradient (100%, 90%, 70%) into distilled water for five minutes each. Slides were next buffered with 1xPBS for 30 minutes, rinsed, and treated with a 60 µM ARCAM-1 solution in 1xPBS for 30 minutes at room temperature. The slides were then rinsed three times with 1xPBS. Slides were coverslipped with DAKO mounting medium (Agilent, Santa Clara, CA, USA).

For immunolabeling of unfixed frozen mouse retina sections with anti-A$\beta$ antibodies, slides were first dried for one hour and then hydrated through an ethanol gradient (100%, 90%, 70%) into distilled water for five minutes each and then let sit in 1xPBS for 15 minutes. Slides were then permeabilized in 1xPBS+0.1% Triton X-100 and blocked with 10% serum for one hour at room temperature. The 6E10 anti-A$\beta$ primary antibody (Covance Cat. SIG-39320, 1:500) was then added onto slides and incubated at 4°C overnight. The following day, slides were rinsed three times with 1xPBS+0.1% Triton X-100 and the secondary antibody added (donkey anti-mouse AlexaFluor594, Abcam Cat. ab150108, 1:2000) for one hour at room temperature. The slides were then rinsed with 1xPBS and coverslipped with DAKO mounting medium containing DAPI.

For staining of formalin-fixed human retina and brain sections, tissues were first embedded in optimal cutting temperature medium and cut using a cryostat to 10 µm thickness. For immunolabeling, slides were dried at 35°C for one hour before rehydrating in 1xPBS for 10 minutes and then placed in 3% hydrogen peroxide for 10 minutes at room temperature and washed once in distilled water. For antigen retrieval, the tissues were placed in 98% formic acid for five minutes at room temperature and then washed with water five times for one minute each. Slides were blocked in TNB blocking buffer (0.1 M Tris-HCl pH 7.5, 0.15 M NaCl and 0.5% TNB (Perkin Elmer FP1012)) for one hour and incubated at 4°C with the primary antibody (6E10, Biolegend Cat. 800701, 1:500 or 4G8, Biolegend Cat. 800701, 1:500) overnight. The next day, slides were rinsed with 1x PBS+0.1% Triton X-100 five times. Slides were then incubated in a humidity chamber at room temperature with the secondary antibody (Biotin goat anti-mouse, Jackson Cat.115-066-072, 1:500) for 45 minutes and washed again in 1xPBS+0.1% Triton X-100 five times and incubated at room temperature with Streptavidin conjugated enzyme conjugate. For DAB and Fast Red staining, tissues were incubated in Streptavidin-HRP (Jackson Cat. 016-030-084, 1:1000) or Streptavidin-AP (Jackson Cat. 016-050-084, 1:1000) dilution for 30 minutes. After washing the slides in 1xPBS+0.1% Triton X-100, contrast stains were preformed following kit protocols (Invitrogen Cat. 00-2020 for DAB and Vector Cat. SK-5105 for

Fast Red). Slides were then counterstained with hematoxylin and dehydrated using an ethanol gradient (50% to 100%), washed in xylene, and sealed with Cytoseal XYL. For ARCAM-1 and Thioflavin-S (ThS) staining, slides were dried at 35°C for one hour before rehydrating in 1x PBS for 10 minutes. Tissues were placed in a humidity chamber and incubated with ARCAM-1 (60 µM in 1xPBS) or ThS (1% solution in 1xPBS) for 30 minutes in the dark and washed with 1x PBS for five minutes three times. Tissues were then counterstained with DAPI (300 nM in 1xPBS) for five minutes, rinsed with 1x PBS, and then mounted with DAKO mounting media.

For ARCAM-1 and ThS staining of formalin-fixed whole-mount human eyes, the globes were first washed with distilled water to remove excess formalin. The cornea-iris complex was then removed with the lens to separate the anterior segment, exposing the eyecup containing the intact retina. Incisions were placed along the four cardinal axes while maintaining the orientation of the retinal fields to create four leaflets (e.g., nasal/temporal and superior/inferior, as determined by position of the optic nerve and superior and inferior rectus muscles). The vitreous humor was removed carefully, and the retina carefully separated by peeling back from the retinal pigment epithelium using a spoon blade and blunt forceps. The retina was then transferred to a large glass microscope slide with the GCL face up and one corner of the superior-temporal leaflet was cut to mark orientation. Whole-mount retinas were floated in 1xPBS and then in 98% formic acid for three minutes before rinsing twice with distilled water for five minutes. The tissue was then placed in 1xPBS for five minutes before mounting onto a glass microscope slide and excess buffer wicked off. ARCAM-1 (60 µM in 1xPBS) or ThS (1% solution in 1xPBS) was added onto slides for 30 minutes and then rinsed three times with 1xPBS. Tissues were then counterstained with DAPI (300 nM in 1xPBS) for three minutes and rinsed three times with 1xPBS. Slides were then mounted with a coverslip with DAKO mounting medium.

## Imaging Stained Eye and Brain Tissues

True color images were obtained on an Olympus MVX10 Macroview equipped with a CCD camera, a long-pass filter (MWB2, Olympus, Tokyo, Japan) and 2× plano apochromatic objective (MVX, Olympus, Tokyo, Japan) with 0.5 NA. Each slide was illuminated with epifluorescence and imaged with an exposure time of 0.2 to 0.8 seconds, depending on the sample. Bright-field images of DAB and Fast Red stains were imaged on an Olympus EX41 equipped with 4×, 10×, 40×, and 60× objectives and a DP controller.

Confocal images were obtained on an Olympus FluoView FV1000 spectral deconvolution confocal microscope with 5% power and a 10x objective. Blue, green, and red channels were imaged using 405 nm, 488 nm, and 534 nm excitation laser lines, respectively. Spectral deconvolution of the emission spectra from stained tissues was measured at 1 nm increments from 450 to 650 nm. For background regions, a minimum of 10 randomly selected areas were measured as a control. The wavelength corresponding to the highest relative fluorescence intensity was taken as the maximum $\lambda_{emission}$. Current offsets to the photomultiplier tube, exposure times, and gain were adjusted during imaging to avoid overexposure and saturation of the fluorescence images. Laser power to the 405 nm excitation line was kept below 5% power, all other lasers were kept below 15% to avoid photobleaching.

## Data Analysis and Image Processing

Fundus images were exported to ImageJ[25] and Image-Pro Premier (MediaCybernetics, Rockville, MD, USA) for quantifying amyloid aggregates. A difference of Gaussian image was created and then contrast adjusted using thresholding in ImageJ to reduce shadowing effects (i.e., alignment deviations during imaging) due to random motion from the mice during imaging. Files were then processed in Image-Pro Premier using a point-based detection parameter where only adjacently localized high-intensity pixels were counted. The area, perimeter, and major and minor axes (assuming an ellipsoid shape) were measured after object detection. For the representative images shown, fundus images were imported into Photoshop 7 (Adobe, San Jose, CA, USA) and an unsharp mask with a 10-pixel radius at 50% was applied.

## Statistics

Spectral measurements are represented as the mean ± standard deviation. For comparisons between two data sets, a nonparametric Mann-Whitney test for two samples was used and the data presented as the mean ± standard deviation. For comparisons between three or more data sets, a Kruskal-Wallis test was performed first to determine statistical differences. Post hoc analyses were then carried out with Dunn's test for statistical significance and the data reported as the mean ± standard deviation. Statistical significance was set at $^{*}P < 0.05$, and $^{**}P < 0.01$.

## Results

### ARCAM-1 Fluorescently Labels Amyloid Plaques in APP/PS1 Mouse and Human AD Brain Tissue

We first evaluated the ability of ARCAM-1 (Fig. 1a) to stain plaques in neuronal tissue. We stained unfixed hippocampal tissue from an APP/PS1 mouse model for AD and unfixed frontal cortex tissue from a human AD patient with ARCAM-1 (Fig. 1b). In both cases, the tissue was illuminated with 488 nm light, and we observed fluorescently stained deposits consistent with dense-core plaques with emission intensities approximately three to five times greater than background and a maximum $\lambda_{emission}$ between 515 and 525 nm (Fig. 1c). We also observed labeling of the vasculature in the human AD brain sections (Supplementary Fig. S1).

### ARCAM-1 Enables Antemortem Labeling of Amyloid Deposits in the Retina of APP/PS1 Mice

ARCAM-1 was next administered to aged APP/PS1 mice via an intraperitoneal (IP) injection and the retinas were imaged at less than 5mW/cm$^2$ using a Phoenix Systems Micron IV fluorescent ophthalmoscope. In contrast to age-matched wild-type (WT) mice, the retina of APP/PS1 mice presenting senile plaque brain pathology showed distinct fluorescent focal deposits that exhibited a ~1.5-fold increase in intensity (compared to the fluorescence of the background tissue) approximately 10 minutes after injection of ARCAM-1 (Fig. 2a and Supplementary Figs. S2–S4). These deposits were observed in four out of eight APP/PS1 mice ranging from 7.5 to 12 months of age (three female and one male, Supplementary Fig. S3) and zero of the three age-matched WT control mice. Fundus images pre- and post-ARCAM-1 injection revealed that mouse 3 exhibited an increase in the number of observable fluorescent deposits postinjection, suggesting that ARCAM-1 not only facilitated, but enabled, the detection of deposits (Supplementary Fig. S4). In mouse 4, however, we observed the same number deposits by fundus imaging pre- and postinjection with ARCAM-1, but the fluorescence intensity of the objects compared to background tissue was greater in the postinjection images compared to in the preinjection images (Supplementary Fig. S4). Processing of the postinjection in vivo fluorescence fundus images using a difference of Gaussian filter (see Fig. 2a and Supplementary Fig. S5 for examples of such processed images) revealed that there was an average of 15.5 ± 1.9 aggregates in the retina of the four mice with positive staining and these deposits appeared on average 7.9 ± 0.2 μm in radius (Supplementary Table S1).

To better characterize these aggregates, we euthanized the mice and examined cross-sections from one of the eyes for staining with ARCAM-1. True color imaging revealed that these fluorescent deposits generally reside in the outer nuclear layer (Fig. 2b and Supplementary Fig. S6) and were approximately 15 to 20 μm in diameter, consistent in size with the deposits visualized from the in vivo retinal scans; additionally, the deposits were immunoreactive with an anti-A$\beta$ antibody (6E10) (Fig. 2b). The other eye was dissected for whole-mount imaging, where the ARCAM-1-labeled deposits were found to be globular in shape (Fig. 2c) with a broad emission profile (Fig. 2d), indicating that deposits were present in both eyes. To rule out that these aggregates were age-dependent lipofuscin deposits commonly found in neuronal tissue, we measured the emission of the deposits labeled with ARCAM-1 (maximum $\lambda_{emission}$ = 517 ± 8 nm) and found the deposits were indeed blue-shifted relative to the known native autofluorescence properties of lipofuscin (550–590 nm).[26,27] Moreover, the results from spectroscopic inspection of these retinal foci were consistent with the spectral properties of ARCAM-1 when bound to amyloid aggregates in the brain (Fig. 1c and Fig. 2d).

### ARCAM-1 Fluorescently Stains Amyloid Deposits in the Retina of Alzheimer's Disease Patients

ARCAM-1 was next evaluated for its capability to fluorescently stain amyloid-containing deposits in human retinal tissue. In retinal whole-mounts from AD patients, staining highlighted fluorescent deposits similar in size and morphology to those seen in the APP/PS1 mouse retinas (Fig. 2c and Fig. 3a). We examined the retina of five patients in total: two cognitively normal, one low-grade AD, and two with severe AD at Braak stage V/VI (Table). In examining the whole-mount retina of these patients, the density and number of fluorescently stained deposits in the retina increased with increasing severity of the disease (i.e., more fluorescent deposits were observed in patients with more advanced AD pathology) (Supplementary Figs. S7–S11). Although these objects were seen in the cognitively normal patients as well, AD patients had two or more times as many labeled deposits (Supplementary Figs. S12a, d), with amyloid deposits having an average radius of 7.5 ± 1.3 μm (Supplementary

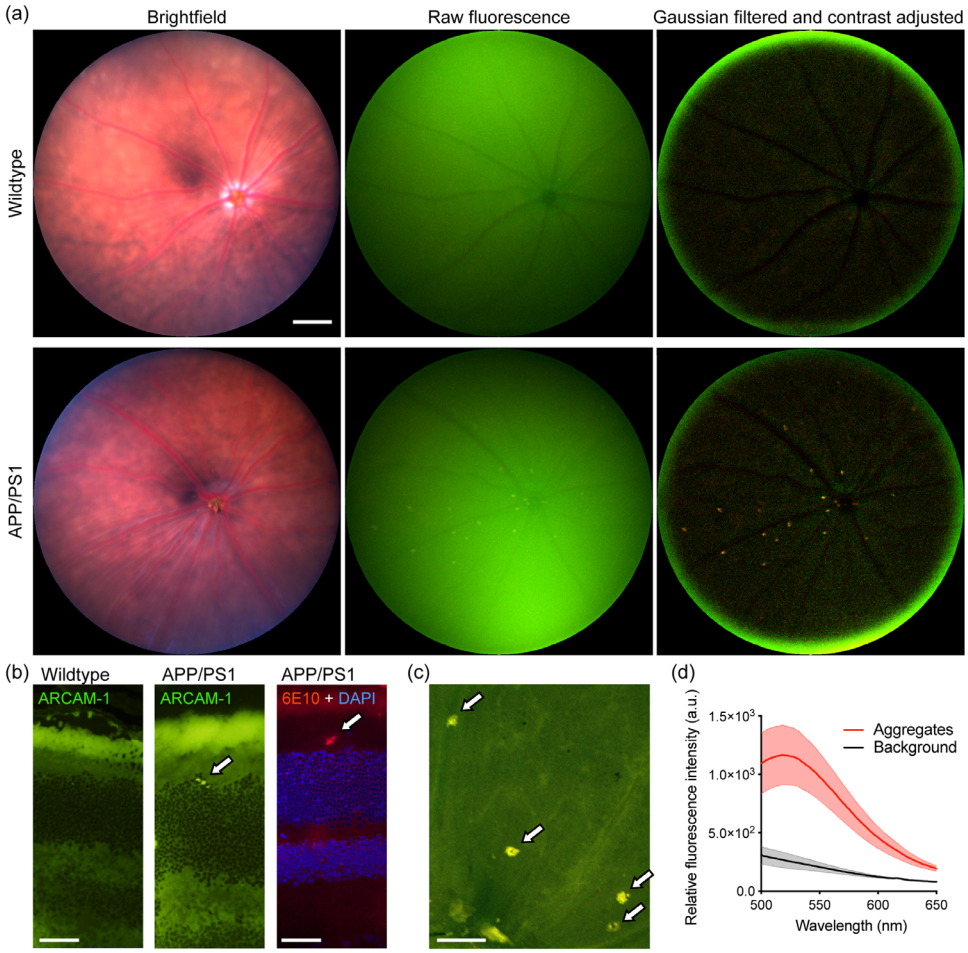


**Figure 2.** ARCAM-1 staining of retinas from a wild-type mouse or a mouse model of Alzheimer's disease. (a) In vivo fundus images from a wild-type and age-matched APP/PS1 AD mouse after an IP administration of ARCAM-1. Rightmost micrographs show Gaussian filtered and contrast adjusted fundus images to highlight fluorescent deposits. Scale bars for full and magnified images = 200 and 100 µm, respectively. The shadowing seen in the brightfield fundus images are due to alignment drift from the objective of the microscope.[41] (b) Cross sections from a wild-type and APP/PS1 mouse stained with ARCAM-1 (true color image shown, see also Supplementary Fig. S3) and 6E10 anti-A$\beta$ antibody (shown with the red and blue confocal channels to highlight the 6E10 staining of an A$\beta$ deposit (red) and the DAPI staining of the nuclei to identify the neuronal layers in the retina (blue)). Scale bars = 50 µm. (c) Confocal images of a whole-mount retina from an APP/PS1 mouse treated antemortem with ARCAM-1. Scale bar = 80 µm. (d) Average fluorescence emission spectra of the aggregates seen in (a) – (c) versus background tissue fluorescence. Maximum $\lambda_{emission}$ of stained aggregates = 517 ± 8 nm. White arrows indicate labeled deposits.

**Table.** Details of Postmortem Human Cases

| Patient | Age | Sex | Brain Neuropathology (NIA ABC Score)[42] |
|---|---|---|---|
| Alzheimer's patient 1 (AD 1) | 71 | M | High level Alzheimer's disease, Braak V/VI (A3 B3 C3) |
| Alzheimer's patient 2 (AD 2) | 82 | F | High level Alzheimer's disease, Braak V/VI (A3 B3 C3) |
| Alzheimer's patient 3 (AD 3) | 85 | M | Low level Alzheimer's disease (A1 B1 C1) |
| Cognitively normal patient 1 (CN 1) | 73 | M | Normal |
| Cognitively normal patient 2 (CN 2) | 74 | M | Normal |

Fig. S12b), similar in size to other reports of human retinal amyloid deposits[5–7,18] and to the deposits seen in APP/PS1 mice (Supplementary Table S2). In the three AD patients, the superior regions of the retina appeared to contain a higher density of labeled aggregates compared to the inferior regions (Supplementary Figs. S12c, e and Supplementary Fig. S13). Furthermore, cross sections of the retina from the two patients with advanced AD pathology (AD1 and AD2) revealed aggregates stained with ARCAM-1 were found in both

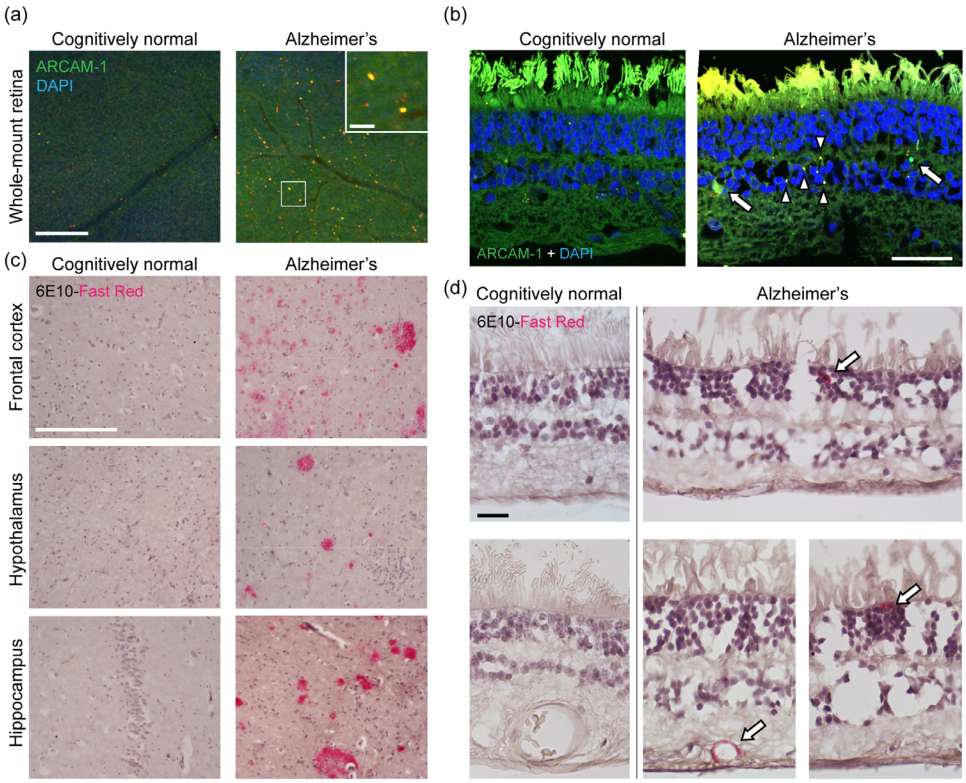


**Figure 3.** ARCAM-1 staining of retina from a cognitively normal human (CN1) and an Alzheimer's disease patient (AD2). (a) Confocal fluorescence micrographs from whole-mount retina stained with ARCAM-1 and counterstained with DAPI. Scale bars for the full and magnified inset = 300 and 50 µm, respectively. (b) Cross sections from the same retina in a) stained with ARCAM-1 and DAPI. White arrows indicate large deposits, while white arrowheads indicate small aggregates. Scale bar = 50 µm. (c) Micrographs of various brain regions from the patients in (a) immunostained with the 6E10 anti-amyloid $\beta$ antibody and visualized with Fast Red. Scale bar = 500 µm. (d) Retinal cross sections labeled with 6E10 and visualized with Fast Red; white arrows indicate positive labeling. Scale bar = 50 µm.

the nuclear and plexiform layers (Fig. 3b and Supplementary Fig. S7 and S8).

Next, we examined the corresponding fixed brain sections from each patient to evaluate the severity of amyloid deposition. Indeed, brain sections from all three AD patients were reactive to anti-A$\beta$ antibodies (6E10 and 4G8), visualized with the Fast Red and DAB chromophores (Fig. 3c and Supplementary Figs. S7–S11). Interestingly, one cognitively normal patient (CN2) had some A$\beta$ plaques in the brain sections as well as some amyloid-containing deposits in retinal whole-mount and cross-sectional staining (Supplementary Fig. S11). Retinal cross sections from the two patients with severe AD brain pathology (AD1 and AD2) and the CN1 patient were also immunostained using the 6E10 anti-A$\beta$ antibody to examine if they had any amyloid-containing deposits. Like the results from ARCAM-1 staining, immunofluorescence staining revealed the presence of amyloid-containing deposits in both the nuclear and plexiform layers from the AD patients (Fig. 3d and Supplementary Fig. S7 and S8). Finally, we stained part of the retinal whole-mounts and cryosections from these human retinas with Thioflavin-S (ThS), a common amyloid-binding histological staining agent,[28] and found similar results as those seen with ARCAM-1 (Supplementary Figs. S7–S11). Of note, immunofluorescent positive reactivity was also found in some vasculature of AD retina cross sections (Fig. 3d), but not in the retinas of the cognitively normal patients (Supplementary Fig. S10 and S11).

## Discussion

The results presented here support the presence of amyloid-containing aggregates in the retinas of an AD mouse model and human AD patients that can be identified using ARCAM-1. Consistent with reports of curcumin labeling amyloid deposits in retinal tissue, our results support the hypothesis that

AD pathology also emerges in the eye. Notably, in contrast to the maximum fluorescence emission wavelength of curcumin when bound to amyloids (~550 nm), utilizing the specific emission signature of ARCAM-1 when bound to amyloid (515–525 nm) allows for identification of the presence of $\beta$-amyloid-containing aggregates in retinal layers that could otherwise be mistaken for common autofluorescence (550–590 nm).[26,27] We also found that the average size of aggregates in the human retina labeled by ARCAM-1 (147.1 ± 32.0 $\mu m^2$, Supplementary Table S1) was smaller than those reportedly labeled by curcumin (~520 $\mu m^2$).[18] When ARCAM-1 was applied to retinas from human patients, we observed an apparent high degree of amyloid-containing aggregates in AD patients compared to healthy controls (Supplementary Figs. S12a, d). Cursory inspection found ARCAM-1–labeled amyloid-containing deposits throughout the retina. Interestingly, there appeared to be a higher density of labeled deposits in the superior region of the retina from AD compared to the superior region of the retina of CN patients, which is consistent with previous reports that suggest that amyloid-containing deposits are more prevalent in the superior region of retinas from AD patients (Supplementary Figs. S12c, e and Supplementary Fig. S13).[6,7] To examine whether these qualitative observations were statistically significant, we treated the number of observed amyloid deposits from multiple 1.6 $mm^2$ image fields of the five patients as either 1) independent measurements or 2) as averaged densities per patient prior to statistical analyses. In the former case, we found that the density of labeled deposits was significantly higher for AD patients compared to control patients, and that there was a significantly higher density of labeled deposits in the superior region of the retina from AD compared to the superior region of the retina of CN patients (Supplementary Figs. S12a, c). However, while we found a similar trend in the data when we first averaged the density of labeled objects per patient, the data did not reach statistical significance (Supplementary Figs. S12d, e). We note, though, that stratifying patients simply as AD or CN does not account for the heterogeneity in the spatial distribution of amyloid-containing deposits in the retina or for differences in the abundance of retinal amyloid-containing deposits that could correlate with disease progression (i.e., the AD classification encompasses a spectrum of the disease from mild to severe). Due to the limited number of samples available for this study, we could not adequately account for these important parameters in our analyses and, thus, our results may not be representative of the general population.

Although this initial study is supportive of the hypothesis that the presence of amyloid deposits can be detected in the retinas of an AD mouse model and in the retinas of human AD patients, there were two technical issues that we encountered with these specimens over the course of this work that should be noted. First, while we were able to observe retinal amyloid deposits in both male and female aged (7.5–12 month) APP/PS1 mice (Supplementary Table S1 and Supplementary S3), such retina deposits were observed only in four of eight mice. These results are consistent with a recent report that found plaque-like deposits in one out of eleven APP/PS1 mice in retinal whole-mounts, and another that examined the 5xFAD mouse model for AD, where the authors were only able to detect retinal deposits in four out of nine mice using retinal cross section immunohistochemistry.[29,30] ARCAM-1 was found to both facilitate the detection of deposits that were observable preinjection (by increasing the fluorescence intensity of objects by ~150% over background after injection compared to before injection) and enable detection of objects that were not observed before injection (for instance, in mouse 3 the number of observed deposits increased from 8 before injection to 17 after injection). However, the observation that any retinal deposits exhibited autofluorescence that could be visualized without fluorescent dyes was surprising, and additional work will be necessary to shed light on the origin of such autofluorescence. We, therefore, caution that neither of these two common AD mouse models of brain amyloid pathology are ideal for examining retinal amyloid pathology, highlighting the need for better animal models for the rapid development of new retinal diagnostic tools for AD. Second, tissue preparation plays a large role in the staining of retinal amyloid deposits by ARCAM-1 or anti-A$\beta$ antibodies. Due to the nature of most amyloid-binding dyes, the preservation of the stacked beta sheet structure of the amyloid is required for binding. Extensive tissue preparation typically used for antigen retrieval from, for example, paraffin-fixed tissue, and often required for antibody staining, may modify the surface of the amyloid structure and prevent the binding of amyloid-targeting dyes.[31] We, therefore, were able to stain amyloid deposits in the brain or retina with either ARCAM-1 or anti-A$\beta$ antibodies (Supplementary Table S3), but costaining was precluded with the formalin-fixed human tissue procured for this study. These findings may have relevance for some of the reported mixed results from groups studying AD pathology in the eye,[7,18,32–37] where using molecular dyes such as congo red or curcumin to detect amyloid deposits in the retina

may have been hampered by the use of aggressive tissue preparation methods, including long tissue fixation periods, stringent washing steps for paraffin embedding, or harsh antigen retrieval protocols (which greatly reduces the secondary and tertiary protein motifs). Thus, there is a fine balance required for tissue preparation to both preserve the amyloid structures for dye binding and to access the epitopes from fixed tissue for antibody detection. While more difficult to acquire, using frozen, unfixed rather than fixed brain and retinal samples may enable more detailed examination of tissue in future studies.

Although our results in mice and human retina revealed a higher density of amyloid-containing aggregates in the outer retinal layers (e.g., the outer nuclear and outer plexiform layers, Figs. 2b, 3b, & 3d), this observation may be, in part, due to the higher density of neurons and synapses in these layers as compared to the inner layers. Furthermore, as noted in other studies, cross section pathology is likely to miss deposits in neuronal layers due to sampling frequency (e.g., the low probability of finding aggregates in a 10 µm thick cross section).[33–35] Specifically, while we did not readily detect amyloid deposits in the GCL, it does not necessarily indicate the absence of these aggregates in the retinal ganglion cells or the nerve fibers. Whole-mount imaging provides a more accurate representation of the spatial distribution of these aggregates across the retina but is limited by the Z-axis resolution due to scattering of emitted fluorescence from layers distal to the objective. Indeed, fundus imaging of the APP/PS1 mice could readily image the surface of the inner retina and was able to detect 15.5 ± 1.9 aggregates from most likely the GCL and NFL, but inspection of the deeper retinal layers showed a higher density of labeled deposits that may have been precluded due to limitations of the fundus camera used in this study (Supplementary Table S1, Supplementary Fig. S6). Additionally, while ARCAM-1 has previously been shown to exhibit excellent specificity and enhanced fluorescence in the presence of amyloid aggregates over serum proteins,[21] the high background fluorescence observed in the mouse retinas after injection suggests that the initial formulation for IP injections used in this study leads to a flooding of the dye into the background retinal tissue. Thus, future work that includes dose-ranging studies and imaging with advanced ophthalmoscopy systems could lead to an improvement in signal-to-noise, enabling even greater fluorescence contrast between the amyloid-containing deposits and background tissue for antemortem imaging.

An interesting finding from the present study is that the behavioral classification of AD did not always match the retinal or brain pathology, as in the case of patient CN2 (Supplementary Fig. S11). Indeed, this patient exhibited amyloid plaque deposition in their frontal cortex and had a higher degree of amyloid-containing aggregates found in the retina in comparison to the other cognitively normal patient CN1 (Supplementary Fig. S10). Additionally, in the two severe AD cases (AD1 and AD2), there was a higher density of ARCAM-1–labeled deposits in the superior region of the retina than in the low-level AD case (AD3, Supplementary Table S2). While much more work is required to examine a potential correlation between amyloid deposition in the brain and retinas in human AD cases, the results presented here are consistent with the idea that amyloid deposition in the brain and retina may precede changes in cognition or memory.

Finally, the presence of amyloid found in the human retinal and brain vasculature (Fig. 3d and Supplementary Fig. S1) presents another potential opportunity for early detection of amyloid-related disease. The retinal vasculature lies in between the cell bodies, with the innermost vessels lying in the NFL, which is the most accessible for optical imaging. Cerebral amyloid angiopathy (CAA) is accompanied by a form of amyloidosis in the neuronal vasculature that is reported to appear in up to 45% of AD patients and is one of the leading causes for hemorrhagic stroke in the elderly.[38] While it is primarily defined by the buildup of amyloid in the small and medium size blood vessels in the brain, case reports have suggested that there are changes to the NFL in patients diagnosed with CAA.[39,40] Thus, our finding that there is amyloid in the inner retinal blood vessels may suggest a link between CAA in the retina and AD pathology that can be identified in a noninvasive way such as with fluorescence imaging. Taken together, our results support the hypothesis of the presence of AD pathology in the eye and highlight a promising opportunity for fluorophore development as new clinical tools for aiding in early-stage diagnosis of AD.

## Acknowledgments

The authors thank the Shiley-Marcos Alzheimer's Disease Research Center at UCSD for providing brain samples from an AD patient with support from the NIH (P30AG062429). We also thank Biogen, in association with their relationship with the University of Miami Brain Endowment Bank, for providing brain and eye matched tissue samples used in this study. Confocal and true-color microscopy was performed at the UC San Diego Microscopy Core in the

Department of Neuroscience with support from the NIH (NS047101).

Funded, in part, by a generous research gift from Amydis, Inc., and by the National Institute on Aging of the National Institutes of Health under Award Numbers R43AG050454, R44AG050454, and RF1AG062362.

Disclosure: **K.J. Cao**, None; **J.H. Kim**, None; **H. Kroeger**, None; **P.M. Gaffney**, None; **J.H. Lin**, None; **C.J. Sigurdson**, advisor of Amydis, Inc.; **J. Yang**, founder, equity interest holder, and advisor of Amydis, Inc.

## References

1. 2020 Alzheimer's disease facts and figures. *Alzheimers Dement*. 2020;16(3):391–460, https://doi.org/10.1002/alz.12068.
2. Matthews KA, Xu W, Gaglioti AH, et al. Racial and ethnic estimates of Alzheimer's disease and related dementias in the United States (2015–2060) in adults aged ≥65 years. *Alzheimers Dement*. 2019;15(1):17–24, https://doi.org/10.1016/j.jalz.2018.06.3063.
3. Kramarow EA, Tejada-Vera B. Dementia mortality in the United States, 2000-2017. *Natl Vital Stat Rep*. 2019;68(2):1–29, https://doi.org/10.1093/geront/gnw162.2167.
4. Dubois B, Hampel H, Feldman HH, et al. Preclinical Alzheimer's disease: definition, natural history, and diagnostic criteria. *Alzheimers Dement*. 2016;12(3):292–323, https://doi.org/10.1016/j.jalz.2016.02.002.
5. La Morgia C, Ross-Cisneros FN, Koronyo Y, et al. Melanopsin retinal ganglion cell loss in Alzheimer disease. *Ann Neurol*. 2016;79(1):90–109, https://doi.org/10.1002/ana.24548.
6. Koronyo Y, Biggs D, Barron E, et al. Retinal amyloid pathology and proof-of-concept imaging trial in Alzheimer's disease. *JCI Insight*. 2017;2(16):e93621, https://doi.org/10.1172/jci.insight.93621.
7. Lee S, Jiang K, McIlmoyle B, et al. Amyloid beta immunoreactivity in the retinal ganglion cell layer of the Alzheimer's eye. *Front Neurosci*. 2020;14:1–14, https://doi.org/10.3389/fnins.2020.00758.
8. Tsai Y, Lu B, Ljubimov AV., et al. Ocular changes in TGF344-AD rat model of Alzheimer's disease. *Invest Ophthalmol Vis Sci*. 2014;55(1):523–534, https://doi.org/10.1167/iovs.13-12888.
9. Javaid FZ, Brenton J, Guo L, Cordeiro MF. Visual and ocular manifestations of Alzheimer's disease and their use as biomarkers for diagnosis and progression. *Front Neurol*. 2016;7:1–11, https://doi.org/10.3389/fneur.2016.00055.
10. O'Brien J, Taylor JP, Ballard C, et al. Visual hallucinations in neurological and ophthalmological disease: pathophysiology and management. *J Neurol Neurosurg Psychiatry*. 2020;91:512–519, https://doi.org/10.1136/jnnp-2019-322702.
11. Danesh-Meyer HV., Birch H, Ku JYF, Carroll S, Gamble G. Reduction of optic nerve fibers in patients with Alzheimer disease identified by laser imaging. *Neurology*. 2006;67(10):1852–1854, https://doi.org/10.1212/01.wnl.0000244490.07925.8b.
12. Hedges TR, Galves RP, Speigelman D, Barbas NR, Peli E, Yardley CJ. Retinal nerve fiber layer abnormalities in Alzheimer's disease. *Acta Ophthalmol Scand*. 1996;74(3):271–275, https://doi.org/10.1111/j.1600-0420.1996.tb00090.x.
13. den Haan J, Verbraak FD, Visser PJ, Bouwman FH. Retinal thickness in Alzheimer's disease: a systematic review and meta-analysis. *Alzheimer's Dement Diagnosis, Assess Dis Monit*. 2017;6(1):162–170, https://doi.org/10.1016/j.dadm.2016.12.014.
14. Hinton DR, Sadun AA, Blanks JC, Miller CA. Optic-nerve degeneration in Alzheimer's disease. *N Engl J Med*. 1986;315(8):485–487, https://doi.org/10.1056/nejm198608213150804.
15. Cunha JP, Proença R, Dias-Santos A, et al. OCT in Alzheimer's disease: thinning of the RNFL and superior hemiretina. *Graefe's Arch Clin Exp Ophthalmol*. 2017;255(9):1827–1835. Published online 2017, https://doi.org/10.1007/s00417-017-3715-9.
16. Krasodomska K, Lubiński W, Potemkowski A, Honczarenko K. Pattern electroretinogram (PERG) and pattern visual evoked potential (PVEP) in the early stages of Alzheimer's disease. *Doc Ophthalmol*. 2010;121(2):111–121. Published online 2010, https://doi.org/10.1007/s10633-010-9238-x.
17. Katz B, Rimmer S, Iragui V, Katzman R. Abnormal pattern electroretinogram in Alzheimer's disease: evidence for retinal ganglion cell degeneration? *Ann Neurol*. Published online 1989, https://doi.org/10.1002/ana.410260207.
18. Koronyo-Hamaoui M, Koronyo Y, Ljubimov AV., et al. Identification of amyloid plaques in retinas from Alzheimer's patients and noninvasive in vivo optical imaging of retinal plaques in a mouse model. *Neuroimage*. 2011;54(Suppl):S204–S217, https://doi.org/10.1016/j.neuroimage.2010.06.020.

19. Yang F, Lim GP, Begum AN, et al. Curcumin inhibits formation of amyloid $\beta$ oligomers and fibrils, binds plaques, and reduces amyloid in vivo. *J Biol Chem*. Published online 2005, https://doi.org/10.1074/jbc.M404751200.
20. Guan Y, Cao KJ, Cantlon A, et al. Real-time monitoring of Alzheimer's-related amyloid aggregation via probe enhancement-fluorescence correlation spectroscopy. *ACS Chem Neurosci*. 2015;6(9):1503–1508, https://doi.org/10.1021/acschemneuro.5b00176.
21. Do JP, Cao KJ, Wei S, Laurent LC, Parast MM, Yang J. Identification of patients with preeclampsia by measuring fluorescence of an amyloid-binding aryl cyano amide in human urine samples. *Anal Chem*. 2018;90(24):14316–14320, https://doi.org/10.1021/acs.analchem.8b03649.
22. Trinchese F, Liu S, Battaglia F, Walter S, Mathews PM, Arancio O. Progressive age-related development of Alzheimer-like pathology in APP/PS1 mice. *Ann Neurol*. 2004;55(6):801–814. Published online 2004, https://doi.org/10.1002/ana.20101.
23. Kerbage C, Sadowsky CH, Tariot PN, et al. Detection of amyloid $\beta$ signature in the lens and its correlation in the brain to aid in the diagnosis of Alzheimer's disease. *Am J Alzheimers Dis Other Demen*. 2015;30(8):738–745, https://doi.org/10.1177/1533317513520214.
24. Cao KJ. Development of Fluorescent Methods for the Detection of Amyloidosis in Neurodegeneration. Published online 2016.
25. Schindelin J, Arganda-Carreras I, Frise E, et al. Fiji: an open-source platform for biological-image analysis. *Nat Methods*. 2012;9(7):676–682, https://doi.org/10.1038/nmeth.2019.
26. Eldred GE, Miller G V., Stark WS, Feeney-Burns L.Lipofuscin: resolution of discrepant fluorescence data. *Science*. 1982;216(4547):757–759, https://doi.org/10.1126/science.7079738.
27. Marmorstein AD, Marmorstein LY, Sakaguchi H, Hollyfield JG. Spectral profiling of autofluorescence associated with lipofuscin, Bruch's membrane, and sub-RPE deposits in normal and AMD eyes. *Invest Ophthalmol Vis Sci*. 2002;43(7):2435–2441.
28. Urbanc B, Cruz L, Le R, et al. Neurotoxic effects of thioflavin S-positive amyloid deposits in transgenic mice and Alzheimer's disease. *Proc Natl Acad Sci USA*. Published online 2002, https://doi.org/10.1073/pnas.222433299.
29. Harper DJ, Augustin M, Lichtenegger A, et al. Retinal analysis of a mouse model of Alzheimer's disease with multicontrast optical coherence tomography. *Neurophotonics*. 2020;7(1):015006, https://doi.org/10.1117/1.nph.7.1.015006.
30. Lim JKH, Li QX, He Z, et al. Retinal functional and structural changes in the 5xFAD mouse model of Alzheimer's disease. *Front Neurosci*. 2020;14:1–13, https://doi.org/10.3389/fnins.2020.00862.
31. Nyström S, Bäck M, Nilsson KPR, Hammarström P. Imaging amyloid tissues stained with luminescent conjugated oligothiophenes by hyperspectral confocal microscopy and fluorescence lifetime imaging. *J Vis Exp*. 2017;20(128):56279, https://doi.org/10.3791/56279.
32. Alber J, Goldfarb D, Thompson LI, et al. Developing retinal biomarkers for the earliest stages of Alzheimer's disease: what we know, what we don't, and how to move forward. *Alzheimers Dement*. 2020;16(1):229–243, https://doi.org/10.1002/alz.12006.
33. den Haan J, Morrema THJ, Verbraak FD, et al. Amyloid-beta and phosphorylated tau in post-mortem Alzheimer's disease retinas. *Acta Neuropathol Commun*. 2018;6:147, https://doi.org/10.1186/s40478-018-0650-x.
34. Ho CY, Troncoso JC, Knox D, Stark W, Eberhart CG. Beta-amyloid, phospho-tau and alpha-synuclein deposits similar to those in the brain are not identified in the eyes of Alzheimer's and Parkinson's disease patients. *Brain Pathol*. 2014;24(1):25–32, https://doi.org/10.1111/bpa.12070.
35. Chidlow G, Wood JPM, Manavis J, Finnie J, Casson RJ. Investigations into retinal pathology in the early stages of a mouse model of Alzheimer's Disease. *J Alzheimers Dis*. 2017;56(2):655–675, https://doi.org/10.3233/JAD-160823.
36. Williams EA, McGuone D, Frosch MP, Hyman BT, Laver N, Stemmer-Rachamimov A. Absence of Alzheimer disease neuropathologic changes in eyes of subjects with Alzheimer disease. *J Neuropathol Exp Neurol*. 2017;76(5):376–383, https://doi.org/10.1093/jnen/nlx020.
37. Schön C, Hoffmann NA, Ochs SM, et al. Long-term in vivo imaging of fibrillar tau in the retina of P301S transgenic mice. *PLoS One*. 2012;7(12):e53547, https://doi.org/10.1371/journal.pone.0053547.
38. Greenberg SM, Bacskai BJ, Hernandez-Guillamon M, Pruzin J, Sperling R, van Veluw SJ. Cerebral amyloid angiopathy and Alzheimer disease — one peptide, two pathways. *Nat Rev Neurol*. 2020;16(1):30–42, https://doi.org/10.1038/s41582-019-0281-2.
39. Vohra R, Hjortshøj TD, Nordling MM, Sørensen TL, Jensen PK, Kolko M. Potential link between sporadic cerebral amyloid angiopathy and vision loss: a case report.

*Acta Ophthalmol*. 2018;96(6):e753–e755, https://doi.org/10.1111/aos.13681.

40. van Etten ES, de Boer I, Steenmeijer SR, et al. Optical coherence tomography detects retinal changes in hereditary cerebral amyloid angiopathy. *Eur J Neurol*. 2020;27(12):2635–2640, https://doi.org/10.1111/ene.14507.
41. Issa PC, Singh MS, Lipinski DM, et al. Optimization of in vivo confocal autofluorescence imaging of the ocular fundus in mice and its application to models of human retinal degeneration. *Invest Ophthalmol Vis Sci*. 2012;53(2):1066–1075, https://doi.org/10.1167/iovs.11-8767.
42. Hyman BT, Phelps CH, Beach TG, et al. National Institute on Aging—Alzheimer's Association guidelines for the neuropathologic assessment of Alzheimer's disease. *Alzheimers Dement*. 2012;8(1):1–13, https://doi.org/10.1016/j.jalz.2011.10.007.